

Sensor Tasking for Detection and Custody of HAMR Objects

Carolin Frueh, Smriti Nandan Paul

School of Aeronautics and Astronautics, Purdue University, West-Lafayette, IN, USA

Hauke Fiedler

German Space Operations Center (GSOC),

Deutsches Zentrum für Luft- und Raumfahrt (DLR, German Aerospace Center), Wessling, Germany

Abstract

High area-to-mass ratio objects (HAMR) are objects that are highly perturbed especially by non-conservative forces such as drag and solar radiation pressure. As a consequence, they are population different orbital regions than low area-to-mass ratio objects. This makes the objects hard to detect. After initial detection those objects are often lost, because standard follow-up times of thirty periods are not sufficient for redetection. This paper applies a sensor tasking and follow-up strategy to the problem of detecting and keeping custody of HAMR objects.

1. INTRODUCTION

High area-to-mass ratio objects (HAMR) have first been detected by Schildknecht et al in 2004 [15, 14]. These objects feature area-to-mass ratios of $2 \text{ m}^2/\text{kg}$ and higher, potentially up to $100 \text{ m}^2/\text{kg}$. The objects have been detected in the geosynchronous region. This unexpected population of objects is highly susceptible to orbital perturbations, especially of non-conservative forces. In the geosynchronous region solar radiation pressure (SRP) leads to perturbations changing the orbital evolution tremendously compared to standard low area-to-mass ratio objects. They reach higher inclinations, beyond the ± 15 degrees. Additionally the drift in the right ascension of the ascending node, does not follow the usual coupling with the inclination [8, 11, 17, 16]. This has consequences for the detection of HAMR objects. They hence populate different regions of the orbital space in the near geosynchronous region. Surveys that solely focus on controlled or low area-to-mass region will not be able to detect many HAMR objects. Because of the larger perturbations, it is also challenging to keep custody of the objects. Uncertain area-to-mass ratios in combination with the large effect that SRP has on the orbits leads to fast growing uncertainties. Area-to-mass ratios are also not necessarily stable but subject to rapid change due to attitude motion and even potential shape of the objects [7, 6, 9]. It is suspected that HAMR objects are created when aging satellites shed parts of their multi-layer insulation materials. Those material sheets then distach from the satellite bus and freely float in space. The materials are very light and highly flexible. Self-shadowing effects quickly leads to rapid attitude motion even under the rigid body assumption.

This paper uses a combined optimized sensor tasking scenario, fusing classical survey and classical follow-up in a unified framework [2, 4, 3, 5]. The methodology is applied to the HAMR detection and cataloging problem. In a first step a theoretical HAMR population is created and illustrated. In a second step this population is used to map out regions of interest in surveys. Using the optimized sensor tasking, a tasking schedule is formed. Using the theoretical HAMR population the performance of the sensor tasking schedule is evaluated.

2. SENSOR TASKING SURVEY AND FOLLOW-UP FRAMEWORK

The framework has been already introduced in previous publications and is only quickly repeated here for the sake of completeness [2, 4, 3, 5]. Building upon previous work, the problem of sensor tasking can be formulated via a cost function that is then optimized for the observation time in the simplified formulation:

$$\begin{aligned} \max A = & \\ & \sum_{g=1}^l \sum_{h=1}^{r_g} \sum_{f=1}^{m_g} \sum_{t_{g,f}=1}^{j_g} \left[\left(\sum_{i=1}^n \mu_{\text{past}}(\alpha_i(t_{g,f}), \delta_i(t_{g,f})) \cdot p(\alpha_i(t_{g,f}), \delta_i(t_{g,f}), \mathbf{o}, t_{g,f}) \cdot d(\alpha_{f,g}, \delta_{f,g}, \alpha_i, \delta_i, t_{g,f}) \right) \right. \\ & \quad \left. + w \cdot k(\alpha_{f,g}, \delta_{f,g}, t_{g,f}) \right] \end{aligned} \quad (1)$$

$$\alpha_{f,g} - \frac{1}{2}\text{FOV} - \alpha_i(t_{g,f}) \leq 0 \quad (2)$$

$$-\alpha_{f,g} - \frac{1}{2}\text{FOV} + \alpha_i(t_{g,f}) \leq 0 \quad (3)$$

$$\delta_{f,g} - \frac{1}{2}\text{FOV} - \delta_i(t_{g,f}) \leq 0 \quad (4)$$

$$-\delta_{f,g} - \frac{1}{2}\text{FOV} + \delta_i(t_{g,f}) \leq 0 \quad (5)$$

$$\mathbf{R} - \sigma(\alpha_i, \dot{\alpha}_i, \delta_i, \dot{\delta}_i, \rho_i, \dot{\rho}_i, \nu) \leq 0 \quad (6)$$

A is the quantity that is sought to be maximized. It is formed via the sums over l different sensors, employed at r_g observation intervals. Under the assumption of a steady repositioning time independently of the actual slewing distance, a fixed number of viewing directions m_g can be visited. Viewing directions are indicated as right ascension $\alpha_i(t_{g,f})$ and declination $\delta_i(t_{g,f})$ of the specific sensor. The assumption is not unreasonable, as most of the time is spent settle the telescope rather than slewing to the new position. j_g are the number of exposures that are made per viewing direction. The first part of the sum is based on concrete object information, when state information is already present, e.g. in an already existing catalog: $p(\alpha_i(t_{g,f}), \delta_i(t_{g,f}), \mathbf{o}, t_{g,f})$ is the probability of detection; details on its computation can be found in [13, 12], the vector \mathbf{o} indicates that the probability of detection depends on the object orientation, and explicitly on the time $t_{g,f}$, e.g. via the sun's position. $\mu_{\text{past}}(\alpha_i(t_{g,f}), \delta_i(t_{g,f}))$ is a function weighting the past observations. It is responsible to trigger a good anomaly spread in the observations, more information can be found in [2, 4, 5]. $d(\alpha_{f,g}, \delta_{f,g}, \alpha_i, \delta_i, t_{g,f})$ is the count of the objects. Via the constraints, only the objects are counted with are in the field of view (FOV) for given viewing directions. Furthermore, an object contributes only to the count d , if its covariance σ is above a given threshold \mathbf{R} . This avoids that objects are observed too often. The count d can be understood as a probabilistic measure, interpreting the constraints not as the object mean to be in the field of view, but rather as the integrated weight of the probability density function that overlaps with the FOV. The second part of the sum is comprised of the weight w , and the surface function $k(\alpha_{f,g}, \delta_{f,g}, t_{g,f})$ indicated the value of certain viewing directions independently from concrete object information. This second part is used before a priori object information is gathered.

Several simplifications are applied. For one, not every single exposure is evaluated, but only the mid exposure time of a given series. Furthermore, viewing directions are ordered on grid points, excluding various viewing directions and allowing to find a finite number of possible viewing directions within any given time frame. A greedy optimizer is applied. For one single sensor with the given simplification, the optimization can be formulated as the following (dropping the functional dependencies for more clarity):

$$\max A = \sum_{f=1}^{m_g} \left[\left(\sum_{i=1}^n \mu_{\text{past}} \cdot p \cdot d \right) + w \cdot k \right] \quad (7)$$

$$\alpha - \frac{1}{2}\text{FOV} - \alpha_i \leq 0 \quad (8)$$

$$-\alpha - \frac{1}{2}\text{FOV} + \alpha_i \leq 0 \quad (9)$$

$$\delta - \frac{1}{2}\text{FOV} - \delta_i \leq 0 \quad (10)$$

$$-\delta - \frac{1}{2}\text{FOV} + \delta_i \leq 0 \quad (11)$$

$$\mathbf{R} - \sigma \leq 0 \quad (12)$$

2.1. Surface k and HAMR Dynamics

In order to define the surface function k the viewing directions of interest have to be defined. This can be done based on the TLE catalog [3, 5]. In contrast to earlier publications, it is sought to establish the surface without relying on an existing catalog but based on first principles only. This is in part also due to the fact that no extensive HAMR catalog does exist. In order to derive our HAMR surface k function, we initialize virtual objects and then average them. The virtual objects are selected as such that they have their origin in the geosynchronous region.

Five different sets of HAMR objects are propagated with 60 individual objects in each set. The objects are placed in the same orbit, but initiated at staggered initial anomalies, spaced six degrees apart. The rational for the same initial

orbital elements is that the geosynchronous region with its small inclinations and eccentricities, the nodes are not well defined. Choosing different orbits gives the appearance of a higher diversity than is actually present in the initial conditions. The orbital elements semi-major axis, eccentricity, inclination, argument of perigee and right ascension of ascending node (RAAN) are chosen as $a_0 = 42'164$ Km, $e_0 = .03$, $i_0 = .1$ degrees, $\omega_0 = 30$ degrees, and $\Omega_0 = 60$ degrees, respectively. The different sets are all propagated to the same final epoch, 12:00:00 UTC, 1st Sept., 2017. The sets are propagated to this final epoch, over an interval of ten, eight, six, four and two years. The AMR values for each set of objects are generated using uniform distribution with values between $2 m^2/Kg$ and $50 m^2/Kg$. The actual values are listed in Tables 1 to 5 in the Appendix.

The propagation is performed using variational equations, based on the expressions from [10], [1] and [17]. The object is modeled as a perfect sphere of one m^2 with a diffuse reflection coefficient taken as 0.8, and no specular reflection. The variational equations are listed here for completeness. Perturbation forces of Earth central force and J_2 gravity, Sun and Moon third body gravity and solar radiation pressure (SRP) are taken into account.

From Merson [10], perturbations in orbital elements due to J_2 term (to first order) of Earth's gravity, over one time period are given as,

$$\Delta a|_{J_2} = 0 \quad (13)$$

$$\Delta e|_{J_2} = 0 \quad (14)$$

$$\Delta i|_{J_2} = 0 \quad (15)$$

$$\Delta \omega|_{J_2} = 2\pi J_2 \left(\frac{R}{p}\right)^2 \cdot 3 \left(1 - \frac{5}{4}f\right) \quad (16)$$

$$\Delta \Omega|_{J_2} = 2\pi J_2 \left(\frac{R}{p}\right)^2 \left(-\frac{3}{2}\right) \cos i \quad (17)$$

where $J_2 = -C_{2,0} = 0.00108$, R is mean equatorial radius of Earth, p is semi-latus rectum of object orbit, and $f = \sin i$.

From Cook [1], perturbations in orbital elements due to third body gravitational force of Sun or Moon, over one orbital period, are given as,

$$\Delta a|_{TB} = 0 \quad (18)$$

$$\Delta e|_{TB} = -\frac{15\pi K e(1-e^2)^{\frac{1}{2}}}{n^2} [AB \cos 2\omega - \frac{1}{2}(A^2 - B^2) \sin 2\omega] \quad (19)$$

$$\Delta i|_{TB} = \frac{3\pi K C}{2n^2(1-e^2)^{\frac{1}{2}}} [A(2 + 3e^2 + 5e^2 \cos 2\omega) + 5Be^2 \sin 2\omega] \quad (20)$$

$$\Delta \Omega|_{TB} = \frac{3\pi K C}{2n^2(1-e^2)^{\frac{1}{2}} \sin i} [5Ae^2 \sin 2\omega + B(2 + 3e^2 - 5e^2 \cos 2\omega)] \quad (21)$$

$$\Delta \omega|_{TB} + \Delta \Omega|_{TB} \cos i = \frac{3\pi K(1-e^2)^{\frac{1}{2}}}{n^2} \left(5 \left[AB \sin 2\omega + \frac{1}{2}(A^2 - B^2) \cos 2\omega \right] - 1 + \frac{3}{2}(A^2 + B^2) \right) \quad (22)$$

where A, B, and C are defined as,

$$A = \cos u_d \cos (\Omega - \Omega_d) + \sin u_d \cos i_d \sin (\Omega - \Omega_d) \quad (23)$$

$$B = \cos i [-\sin (\Omega - \Omega_d) \cos u_d + \cos i_d \sin u_d \cos (\Omega - \Omega_d)] + \sin i \sin u_d \sin i_d \quad (24)$$

$$C = \sin i [\cos u_d \sin (\Omega - \Omega_d) - \sin u_d \cos i_d \cos (\Omega - \Omega_d)] + \cos i \sin i_d \sin u_d \quad (25)$$

$$(26)$$

where i_d , Ω_d , u_d stand for Sun orbit inclination, Sun orbit right ascension of the ascending node, and Sun argument of latitude in the Earth-centered inertial (ECI) frame. In the expressions for A, B, and C, Moon orbit inclination, Moon orbit RAAN, and Moon argument of perigee needs to be used while computing the effect due to gravitational force of Moon. K is defined as,

$$K = \frac{GM_{S/M}}{r_{S/M}^3} \quad (27)$$

where G is universal gravitational constant, $M_{S/M}$ represents Moon or Sun mass depending on whose gravitational effect is being computed, $r_{S/M}$ is the distance of either Moon or Sun from the center of Earth. From Cook [1], perturbations in orbital elements due to SRP over one orbital period, are given as,

$$\begin{aligned}\Delta a|_{SRP} &= -\frac{2F}{n^2 a} \left[(A \sin \omega - B \cos \omega)(r_A \sin \theta_A^* - r_D \sin \theta_D^*) + \right. \\ &\quad \left. (A \cos \omega + B \sin \omega) \left(\frac{r_A - r_D}{e} \right) \right] \quad (28)\end{aligned}$$

$$\begin{aligned}\Delta e|_{SRP} &= \frac{T_p}{\mu} \left[3a^2(1-e^2)^{\frac{1}{2}} \left(\tan^{-1} \left[\frac{(1-e^2)^{\frac{1}{2}} \tan \frac{\theta_A^*}{2}}{1+e} \right] - \tan^{-1} \left[\frac{(1-e^2)^{\frac{1}{2}} \tan \frac{\theta_D^*}{2}}{1+e} \right] \right) - \right. \\ &\quad \left. \frac{1}{2e} (r_A^2 \sin \theta_A^* - r_D^2 \sin \theta_D^*) + \frac{a}{2e} (1-4e^2) (r_A \sin \theta_A^* - r_D \sin \theta_D^*) \right] - \\ &\quad \frac{S_p}{2\mu} \left[(r_A^2 - r_D^2) + \frac{a(1-e^2)}{e^2} (r_A - r_D) + \frac{1}{e} (r_A^2 \cos \theta_A^* - r_D^2 \cos \theta_D^*) \right] \quad (29)\end{aligned}$$

$$\begin{aligned}\Delta i|_{SRP} &= \frac{W}{\mu} \left[\left(\frac{1}{2(1-e^2)} (r_A^2 \sin \theta_A^* - r_D^2 \sin \theta_D^*) + \frac{a(1+2e^2)}{2(1-e^2)} (r_A \sin \theta_A^* - r_D \sin \theta_D^*) - \right. \right. \\ &\quad \left. \left. \frac{3a^2 e}{(1-e^2)^{\frac{1}{2}}} \left(\tan^{-1} \left[\frac{(1-e^2)^{\frac{1}{2}} \tan \frac{\theta_A^*}{2}}{1+e} \right] - \tan^{-1} \left[\frac{(1-e^2)^{\frac{1}{2}} \tan \frac{\theta_D^*}{2}}{1+e} \right] \right) \right) \cos \omega - \right. \\ &\quad \left. \frac{1}{2e} (r_A^2 - r_D^2) \sin \omega \right] \quad (30)\end{aligned}$$

$$\begin{aligned}\Delta \Omega|_{SRP} &= \frac{W}{\mu \sin i} \left[\frac{(r_A^2 - r_D^2)}{2e} \cos \omega + \right. \\ &\quad \left[\frac{r_A^2 \sin \theta_A^* - r_D^2 \sin \theta_D^*}{2(1-e^2)} + \frac{1+2e^2}{2(1-e^2)} (ar_A \sin \theta_A^* - ar_D \sin \theta_D^*) \right. \\ &\quad \left. \left. - \frac{3a^2 e}{\sqrt{1-e^2}} \left(\tan^{-1} \left(\frac{\sqrt{1-e^2} \tan \frac{\theta_A^*}{2}}{1+e} \right) - \tan^{-1} \left(\frac{\sqrt{1-e^2} \tan \frac{\theta_D^*}{2}}{1+e} \right) \right) \right] \sin \omega \right] \quad (31)\end{aligned}$$

$$\begin{aligned}\Delta \omega|_{SRP} + \Delta \Omega|_{SRP} \cos i &= -\frac{S_p}{\mu e} \left[3a^2 \sqrt{1-e^2} \left(\tan^{-1} \left(\frac{\sqrt{1-e^2} \tan \frac{\theta_A^*}{2}}{1+e} \right) - \tan^{-1} \left(\frac{\sqrt{1-e^2} \tan \frac{\theta_D^*}{2}}{1+e} \right) \right) + \right. \\ &\quad \left. \frac{1}{2e} (r_A^2 \sin \theta_A^* - r_D^2 \sin \theta_D^*) - \frac{a}{2e} (1+2e^2) (r_A \sin \theta_A^* - r_D \sin \theta_D^*) \right] + \\ &\quad \frac{T_p}{2\mu e^3} \left[e(r_A^2 \cos \theta_A^* - r_D^2 \cos \theta_D^*) + a(1-e^2) (r_A - r_D) \right] \quad (32)\end{aligned}$$

where μ represents Earth gravitational parameter, and n represents object mean motion. θ_D^* and θ_A^* are the true anomaly values when the body leaves the Earth's shadow and the true anomaly value when the body enters the Earth's shadow, respectively; r_A and r_D are the corresponding values of object distance from the center of Earth. F and W are defined through following relations,

$$F = -\frac{1}{m} \left(\frac{S_c}{c} \right) \left(\frac{A_\oplus}{r_{so}} \right)^2 4\pi r_b^2 \left(\frac{1}{4} + \frac{C_d}{9} \right) \quad (33)$$

$$W = FC \quad (34)$$

where m is object mass, S_c is solar constant, c is speed of light in vacuum, A_\oplus is astronomical unit, r_{so} is sun-object distance, r_b is object radius, and C_d is diffuse reflection coefficient.

S_p and T_p appearing in Eqs. 28 to 32 are defined as:

$$S_p = F(A \cos \omega + B \sin \omega) \quad (35)$$

$$T_p = F(-A \sin \omega + B \cos \omega) \quad (36)$$

The following approximations have been applied in the analytic expressions. Moon positions analytic approximations have been used [18]. For the shadow passes, the derivation of Valk and Lemaître [17] has been used, applying the

necessary corrections outlined below. The shadow locations are obtained by solving the bi-quadratic equation:

$$A_4 y_l^4 + A_3 y_l^3 + A_2 y_l^2 + A_1 y_l + A_0 = 0 \quad (37)$$

where $y_l = \sin V$, with the true longitude $V = \theta^* + \omega + \Omega$. Of the multiple true longitude values obtained as solutions to Eq. (37), only two values will meet the shadow constraints; these values correspond to the two shadow-sunlight boundaries. The criteria for rejecting other solutions are discussed below. The coefficients A_0, A_1, A_2, A_3, A_4 are given as,

$$A_0 = R^4 k_e^4 - 2R^4 k_e^2 + R^4 + 2R^2 \beta^2 k_e^2 p^2 + 2R^2 \beta^2 p^2 - 2R^2 k_e^2 p^2 - 2R^2 p^2 + \beta^4 p^4 - 2\beta^2 p^4 + p^4 \quad (38a)$$

$$A_1 = -4R^4 h_e k_e^2 + 4R^4 h_e + 4R^2 \beta^2 h_e p^2 - 8R^2 \beta k_e p^2 \xi - 4R^2 h_e p^2 \quad (38b)$$

$$A_2 = -2R^4 h_e^2 k_e^2 + 6R^4 h_e^2 - 2R^4 k_e^4 + 2R^4 k_e^2 + 2R^2 \beta^2 h_e^2 p^2 - 4R^2 \beta^2 k_e^2 p^2 - 2R^2 \beta^2 p^2 - 8R^2 \beta h_e k_e p^2 \xi - 2R^2 h_e^2 p^2 + 2R^2 k_e^2 p^2 \xi^2 + 2R^2 k_e^2 p^2 + 2R^2 p^2 \xi^2 - 2\beta^4 p^4 - 2\beta^2 p^4 \xi^2 + 2\beta^2 p^4 - 2p^4 \xi^2 \quad (38c)$$

$$A_3 = 4R^4 h_e^3 + 4R^4 h_e k_e^2 - 4R^2 \beta^2 h_e p^2 + 8R^2 \beta k_e p^2 \xi + 4R^2 h_e p^2 \xi^2 \quad (38d)$$

$$A_4 = R^4 h_e^4 + 2R^4 h_e^2 k_e^2 + R^4 k_e^4 - 2R^2 \beta^2 h_e^2 p^2 + 2R^2 \beta^2 k_e^2 p^2 + 8R^2 \beta h_e k_e p^2 \xi + 2R^2 h_e^2 p^2 \xi^2 - 2R^2 k_e^2 p^2 \xi^2 + \beta^4 p^4 + 2\beta^2 p^4 \xi^2 + p^4 \xi^4 \quad (38e)$$

These coefficients are corrected, and are different from the published version in Valk and Lemaitre [17]. Parameters k_e , h_e , β , ξ appearing in Eq. (38) are defined as follows,

$$k_e = e \cos(\omega + \Omega) \quad (39a)$$

$$h_e = e \sin(\omega + \Omega) \quad (39b)$$

$$\beta = X_{\oplus} f_x + Y_{\oplus} f_y + Z_{\oplus} f_z \quad (39c)$$

$$\xi = X_{\oplus} g_x + Y_{\oplus} g_y + Z_{\oplus} g_z \quad (39d)$$

where $X_{\oplus}, Y_{\oplus}, Z_{\oplus}$ represent normalized ECI components of Sun position. $f_i (i = x, y, z)$ and $g_j (i = x, y, z)$ are defined as,

$$\begin{bmatrix} f_x \\ f_y \\ f_z \end{bmatrix} = \begin{bmatrix} \frac{1-p_e^2+q_e^2}{1+p_e^2+q_e^2} & \frac{2p_e q_e}{1+p_e^2+q_e^2} & \frac{-2p_e}{1+p_e^2+q_e^2} \end{bmatrix}^T \quad (40a)$$

$$\begin{bmatrix} g_x \\ g_y \\ g_z \end{bmatrix} = \begin{bmatrix} \frac{2p_e q_e}{1+p_e^2+q_e^2} & \frac{1+p_e^2-q_e^2}{1+p_e^2+q_e^2} & \frac{2q_e}{1+p_e^2+q_e^2} \end{bmatrix}^T \quad (40b)$$

where $p_e = \tan(\frac{i}{2}) \sin \Omega$, $q_e = \tan(\frac{i}{2}) \cos \Omega$, and $[\cdot]^T$ denotes matrix transpose.

The undesirable solutions of the bi-quadratic equation represented by Eq. (37) are rejected using the constraint:

$$\beta \cos V + \xi \sin V < 0 \quad (41)$$

where the above constraint comes from geometrical consideration of the cylindrical shadow model as given in [17]. $x_l = \sin V$ (appearing in Eq. (41)) is obtained by solving the following equation,

$$a_2 x_l^2 + a_1 x_l + a_0 = 0 \quad (42)$$

where the coefficients a_0, a_1 and a_2 are given as,

$$a_0 = p^2 \xi^2 y_l^2 + R^2 + R^2 h_e^2 y_l^2 + 2h_e y_l R^2 - p^2 \quad (43a)$$

$$a_1 = 2p^2 \beta \xi y_l + 2k_e R^2 + 2k_e h_e R^2 y_l \quad (43b)$$

$$a_2 = p^2 \beta^2 + R^2 k_e^2 \quad (43c)$$

These coefficients are corrected, and are different from Valk et al.[17]. In addition to Eq. (41) as constraint, constraints were also put on removing double roots, x_l and y_l being within the range [-1,1], in order to ensure that we get exactly two roots by solving Eq. (37). Once the two values of true longitudes are obtained, the corresponding true anomaly values are quickly computed using known orbit mechanics relations, and subsequently they are used in the SRP perturbation equations.

The final orbital elements for all the HAMR objects are given in Fig. 1. The initial (points) and final objects (stars) in Cartesian coordinate frame are shown in Fig. 2. One can clearly see the rapid inclination gain of the HAMR objects. Furthermore, the objects also gain in eccentricity.

In order to generate the input surface k , the objects have been propagated over a 24 hour period and their positions averaged. A crucial point is the frame in which to represent the surface. A frame in which the apparent motion of the objects is smallest is most advantageous as in the process of time averaging. That way the weight of the single objects is not spread over several positions, but marks one specific viewing direction. In our case in the near GEO region, an azimuth elevation frame has been chosen. It is illustrated for the chosen objects in Fig.3 for the Zimmerwald station. Fig?? a) shows the surface in the topocentric equatorial frame in right ascension and declination, for illustration purposes. Fig?? b) shows the same surface in the local horizon frame, azimuth elevation frame. It can be seen that the HAMR population is shifted towards the standard population present e.g. in the TLE catalog. Inclinations are higher, and the node lines are significantly shifted. This leads to the fact that in the azimuth elevation frame, at least for the Zimmerwald location, the dense inclined object population is below the horizon.

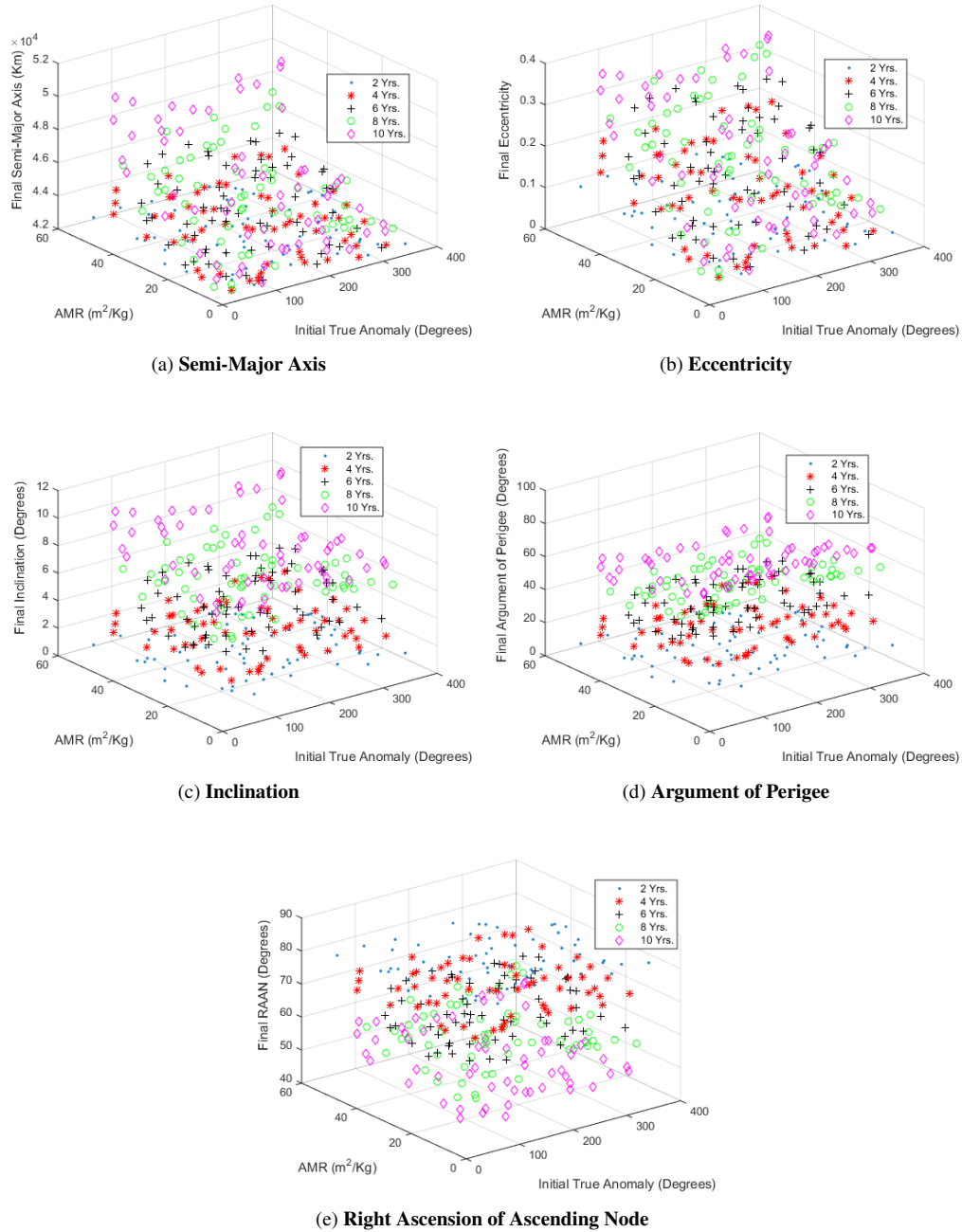


Figure 1: Orbital element evolution over the propagation periods.

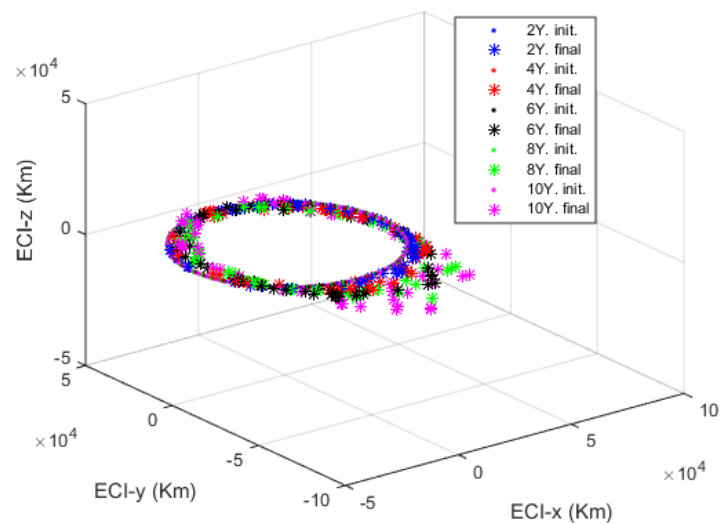


Figure 2: Initial and Final Orbits.

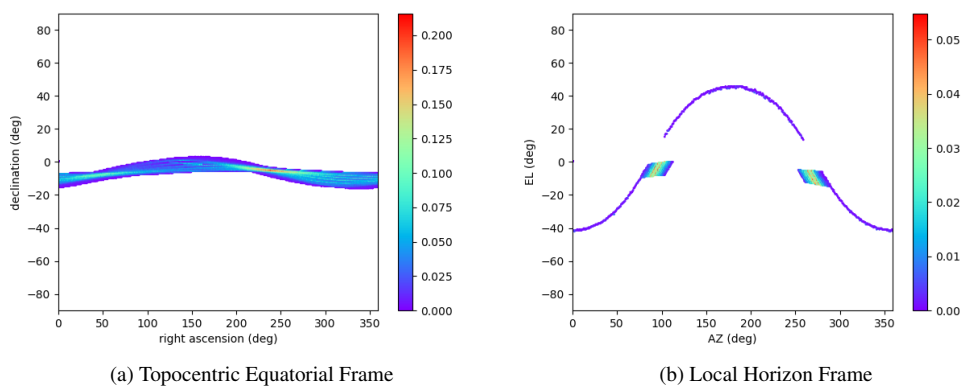


Figure 3: HAMR Surface k relative to SMARTnet™AIUB location Zimmerwald, Switzerland.

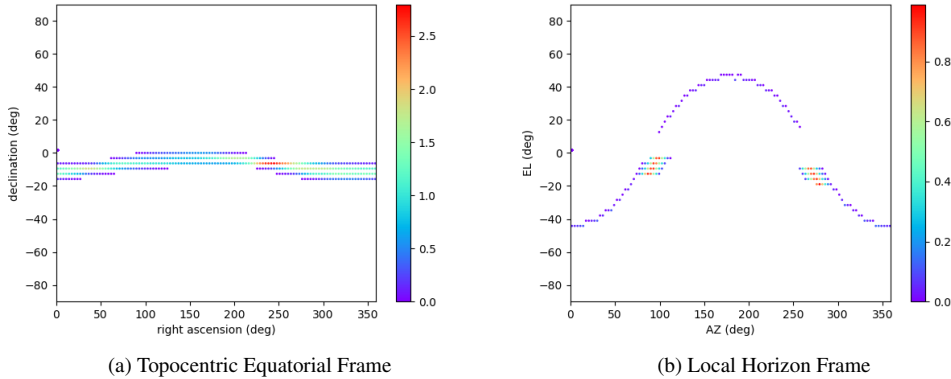


Figure 4: Gridded HAMR Surface k relative to SMARTnet™ and AIUB location Zimmerwald, Switzerland for a 3.77 degree field of view.

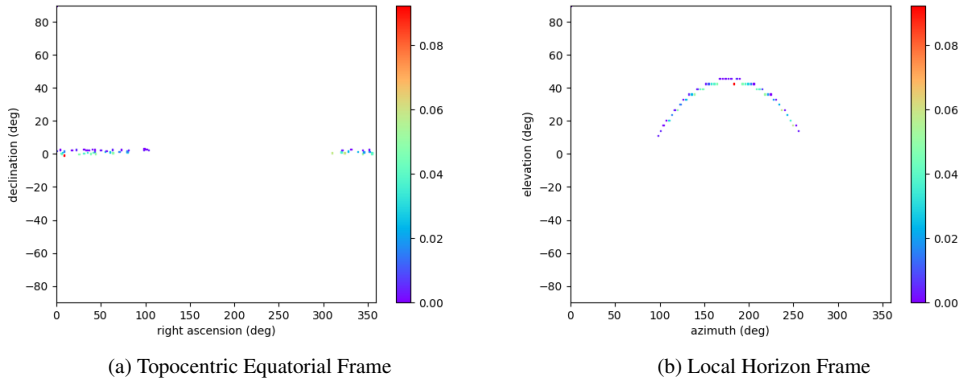


Figure 5: Chosen viewing directions for the SMARTnet™ and AIUB location Zimmerwald, Switzerland, for the night of Sep 1.

3. SIMULATION RESULTS

Using the simplifications outlined above, the observations frame is projected on a grid just under the size of the field of view, such that it maps gaplessly 360 degrees. For the simulations, the SMARTnet™ location of the Astronomical Institute of the University of Bern (AIUB), located in Zimmerwald, Switzerland is used. Seven single images are taken per viewing direction, two detections per object are needed at minimum to account for a successful detection. The simulations are done for the night of Sep 1, 2017. The field of view (FOV) is 3.77 degrees for the chosen setup of the Zimmerwald station. A probability of detection of one has been assumed. The input surface are shown in Fig.4, which is basically the grid point projection of the smooth surface displayed in Fig.3. The grid points are in this case spaced by 3.75 degrees for the given FOV, hence a 0.02 degree overlap exists in the actual observations of neighboring viewing directions. When the method is applied, there are two different modes in which it can be operated. In the first mode, just the surface is used as an input, in the second mode, objects that have been successfully detected are followed up immediately. Using the surface as the input, Fig.4 illustrates the optimizer chosen direction within the observation night starting at Sep. 1 at 18 ,h 59 minutes UTC, at dusk, and at 4 45 minutes the next day at dawn. It can easily be seen that the optimizer follows the input surface, just limited by local horizon. Whereas the chosen directions are significantly different for scenarios with many objects that are up for detection, the chosen directions do not differ significantly, when follow-up observations within the optimization framework are sought. For the observation night, comprising of just short of 586 minutes, only about 20 percent are used for the observations in the surface only scenario, which leaves plenty of time for follow-up obvervations. All but two of the visible objects are re-discovered in the optimized observation scenario. If the option is chosen to enter the newly detected objects into the optimizer, only about 30 percent of the observation time are used, providing two observations for all but one of the detected objects. In a real scenario, the left over time, would be used to

survey or follow-up further objects and regions of interest, such that the TLE objects and catalog as outlined in [3, 5]. It also has to be noted, that uncertainties grow faster for HAMR objects, which leads to shorter re-observation times when spanning the scenario over several nights, in order to keep them in the catalog.

4. CONCLUSIONS

In this paper, a flexible tasking scheme has been introduced: Multiple sensors with different characteristics can be included in an overall optimized scheme. The scheme combines what is known as classical survey and follow-up observations in an automated manner, avoiding a rigid sensor tasking. The system can be started from scratch, leading to automated catalog build-up and maintenance from scratch in a sensing network. In the current work a focus has been laid on high area-to-mass ratio objects. A population which is highly perturbed and as a result hard to detect and keep in a catalog. As no catalog information on those objects is available, variational equations have been used to generate an a priori high area-to-mass ratio input population, starting out from the geostationary ring and assuming a dissemination of HAMR objects in a uniform manner. Populations of 300 objects have been propagated up to 10 years in two year intervals. The resulting distribution significantly differs from the standard TLE population. Averaging the input population lent the input to start the optimization procedure. First results show, that indeed a large number of the visible objects can be detected based on the surface input, but also that the Zimmerwald station that has been used as an example suffers extreme visibility constraints in the example that has been chosen. Future work includes the validation using actual observations with the SMARTnet™ sensors and the Purdue Optical Ground Station.

ACKNOWLEDGMENTS

This work has been supported by GSOC, DLR, 2017 in the SMARTnet™ project.

REFERENCES

1. G.E. Cook. Luni-solar perturbations of the orbit of an earth satellite. *Geophysical Journal International*, 6(3):271 – 291, 1961.
2. C. Frueh. Realistic Sensor Tasking Strategies. In *Advanced Maui Optical and Space Surveillance Technologies Conference (AMOS)*, September 2016.
3. C. Frueh. Fusing Survey and Follow-up for SSA Sensor Tasking. In *AAS/AIAA Astrodynamics Specialist Conference, Stevenson, WA*, 2017. 17-769.
4. C. Frueh. Sensor Tasking for Multi-Sensor Space Object Surveillance. In *Proceedings of the Seventh European Conference on Space Debris, ESOC, Darmstadt, Germany, 18-21 April 2017*, 2017.
5. C. Frueh, H. Fiedler, and J. Herzog. Optimized Realistic Sensor Tasking and Observation Strategies with Exemplification for the Geosynchronous TLE Objects. *Journal of Guidance, Control and Dynamics*, submitted, 2017.
6. C. Früh and M. Jah. Coupled orbit-attitude motion of high area-to-mass ratio (hamr) objects including efficient self-shadowing. *Acta Astronautica*, 95:227–241, 2014.
7. C. Früh, T. Kelecy, and M. Jah. Coupled orbit-attitude dynamics of high area-to-mass ratio (HAMR) objects: Influence of solar radiation pressure, earth's shadow and the visibility in light curves. *Celestial Mechanics and Dynamical Astronomy*, 117:385–404, 2013.
8. J.-C. Liou and J.K. Weaver. Orbital Dynamics of High Area-to-Mass Ratio Debris and Their Distribution in the Geosynchronous Region. In *Proceedings of the Forth European Conference on Space Debris, pp. 119-124, ESOC, Darmstadt, Germany, 18-20 April 2005*, 2005.
9. J.W. McMahon and D.J. Scheeres. A new navigation force model for solar radiation pressure. *Journal of Guidance, Control, and Dynamics*, 33(5):1418–1428, 2010.
10. R.H. Merson. The motion of a satellite in an axi-symmetric gravitational field. *Geophysical Journal International*, 4(SO):17 – 52, 1961.
11. C. Pardini and L. Anselmo. Long-Term Evolution of Geosynchronous Orbital Debris with High Area-to-Mass Ratios. *Trans. Japan Soc. Aero. Space Sci.*, 51:22–27, 2008.
12. F. Sanson and C. Frueh. Noise Quantification in Optical Observations of Resident Space Objects for Probability of Detection and Likelihood. In *AAS/AIAA Astrodynamics Specialist Conference, Vail, CO*, 2015. 15-634.

13. F. Sanson and C. Frueh. Improved ccd equation and probability of detection. *Journal of Astronautical Sciences*, 2016.
14. T. Schildknecht, R. Musci, M. Ploner, G. Beutler, J. Kuusela, J. de León Cruz, and L. de Fatima Domínguez Palmero. Optical Observations of Space Debris in GEO and in Highly-Eccentric Orbits. *Advances in Space Research*, 34(5):901–911, 2004.
15. T. Schildknecht, R. Musci, M. Ploner, W. Flury, J. Kuusela, J. de León Cruz, and L. de Fatima Domínguez Palmero. An Optical Search for Small-Size Debris in GEO and GTO. In *Proceedings of the 2003 AMOS Technical Conference, 9-12 September 2003, Maui, Hawaii, USA*, 2003.
16. S. Valk, N. Delsate, A. Lemaître, and T. Carletti. Global dynamics of high area-to-mass ratios GEO space debris by means of the MEGNO indicator. *Advances in Space Research*, 43(10):1509–1526, 2008.
17. S. Valk and A. Lemaître. Semi-Analytical Investigations of High Area-to-Mass Ratio geosynchronous Space Debris Including Earth’s Shadowing Effects. *Advances in Space Research*, 42(8):1429–1443, 2008.
18. D. Vallado and W. McCain. *Fundamentals of Astrodynamics and Applications*. Microcosm Press, El Segundo, California, 2001. ISBN 0-7923-6903-3.

APPENDIX

The AMR values for the HAMR object simulation in the five sets are listed in the following tables.

(1)35.08	(13)7.12	(25)10.73	(37)21.29	(49)18.21
(2)37.91	(14)48.17	(26)14.66	(38)5.65	(50)45.20
(3)23.63	(15)2.22	(27)8.99	(39)13.52	(51)19.72
(4)6.02	(16)39.20	(28)8.53	(40)7.92	(52)7.34
(5)12.99	(17)41.23	(29)43.73	(41)10.83	(53)39.45
(6)45.84	(18)43.70	(30)29.83	(42)13.52	(54)20.71
(7)9.31	(19)6.05	(31)28.39	(43)22.03	(55)13.60
(8)41.64	(20)21.19	(32)8.96	(44)4.38	(56)21.39
(9)27.84	(21)14.47	(33)42.95	(45)45.33	(57)6.63
(10)49.81	(22)40.40	(34)31.86	(46)47.35	(58)8.33
(11)5.75	(23)22.71	(35)18.85	(47)25.56	(59)47.22
(12)23.25	(24)45.71	(36)26.64	(48)25.48	(60)47.89

Table 1: **Area-to-Mass Ratios (in $\frac{m^2}{kg}$) of the HAMR Objects for 10-Year Propagation**

(1)29.61	(13)28.26	(25)25.37	(37)18.83	(49)12.84
(2)4.87	(14)16.22	(26)22.92	(38)47.07	(50)10.19
(3)13.27	(15)37.75	(27)23.45	(39)44.05	(51)12.93
(4)18.95	(16)11.07	(28)16.70	(40)28.41	(52)22.91
(5)41.42	(17)34.97	(29)26.41	(41)31.88	(53)16.93
(6)2.74	(18)10.81	(30)26.52	(42)30.18	(54)46.32
(7)4.07	(19)19.69	(31)41.25	(43)11.97	(55)22.65
(8)10.11	(20)32.03	(32)40.15	(44)16.46	(56)10.87
(9)33.16	(21)39.45	(33)32.93	(45)24.60	(57)45.43
(10)37.12	(22)5.89	(34)20.17	(46)13.06	(58)49.03
(11)33.09	(23)46.61	(35)40.96	(47)42.53	(59)23.07
(12)23.64	(24)39.23	(36)27.58	(48)11.35	(60)7.33

Table 2: **Area-to-Mass Ratios (in $\frac{m^2}{kg}$) of the HAMR Objects for 8-Year Propagation**

(1)14.39	(13)6.10	(25)27.01	(37)6.74	(49)44.76
(2)21.62	(14)14.60	(26)13.12	(38)14.57	(50)18.04
(3)30.56	(15)40.45	(27)25.47	(39)18.10	(51)35.54
(4)14.59	(16)3.40	(28)31.95	(40)34.63	(52)11.49
(5)30.94	(17)46.58	(29)34.60	(41)8.55	(53)3.47
(6)36.14	(18)37.06	(30)20.98	(42)36.62	(54)37.72
(7)12.64	(19)25.45	(31)19.64	(43)7.12	(55)26.00
(8)7.64	(20)29.77	(32)49.42	(44)33.38	(56)25.04
(9)16.24	(21)13.39	(33)3.81	(45)25.72	(57)45.43
(10)17.30	(22)24.02	(34)44.49	(46)39.39	(58)31.27
(11)22.36	(23)48.23	(35)45.84	(47)36.32	(59)31.65
(12)26.38	(24)28.25	(36)40.22	(48)45.38	(60)43.25

Table 3: **Area-to-Mass Ratios (in $\frac{m^2}{kg}$) of the HAMR Objects for 6-Year Propagation**

(1)40.66	(13)4.86	(25)48.70	(37)4.90	(49)19.88
(2)29.68	(14)34.73	(26)33.15	(38)21.16	(50)11.51
(3)10.78	(15)4.04	(27)40.42	(39)27.29	(51)25.51
(4)13.52	(16)5.43	(28)23.78	(40)22.01	(52)18.30
(5)44.55	(17)27.04	(29)22.75	(41)33.53	(53)47.68
(6)3.38	(18)6.64	(30)41.62	(42)32.14	(54)46.18
(7)25.52	(19)41.27	(31)6.01	(43)16.02	(55)4.53
(8)10.06	(20)41.24	(32)8.39	(44)22.72	(56)37.42
(9)48.98	(21)36.68	(33)10.32	(45)2.74	(57)14.92
(10)36.21	(22)9.19	(34)20.77	(46)49.24	(58)22.30
(11)26.02	(23)33.66	(35)41.91	(47)10.02	(59)28.30
(12)24.61	(24)26.89	(36)40.56	(48)7.10	(60)47.25

Table 4: **Area-to-Mass Ratios (in $\frac{m^2}{kg}$) of the HAMR Objects for 4-Year Propagation**

(1)22.05	(13)3.56	(25)11.16	(37)41.57	(49)22.41
(2)49.19	(14)28.94	(26)22.56	(38)49.17	(50)17.01
(3)16.47	(15)44.33	(27)25.14	(39)37.05	(51)9.75
(4)35.65	(16)34.12	(28)7.79	(40)18.51	(52)10.58
(5)33.98	(17)11.14	(29)30.30	(41)30.04	(53)22.30
(6)27.88	(18)19.71	(30)12.86	(42)7.17	(54)6.52
(7)35.51	(19)24.11	(31)20.46	(43)45.50	(55)30.73
(8)33.99	(20)49.12	(32)29.98	(44)44.22	(56)24.60
(9)10.55	(21)9.51	(33)14.09	(45)41.25	(57)35.41
(10)8.14	(22)43.07	(34)15.94	(46)14.51	(58)35.59
(11)49.96	(23)32.95	(35)31.62	(47)30.53	(59)32.65
(12)10.21	(24)20.06	(36)14.73	(48)3.08	(60)3.61

Table 5: **Area-to-Mass Ratios (in $\frac{m^2}{kg}$) of the HAMR Objects for 2-Year Propagation**